



# Novel photocatalyst incorporating Ni-Co layered double hydroxides with P-doped CdS for enhancing photocatalytic activity towards hydrogen evolution

Songsong Li<sup>a,b,1</sup>, Lu Wang<sup>a,1</sup>, YanDong Li<sup>b</sup>, Linhe Zhang<sup>b</sup>, Aixia Wang<sup>b</sup>, Nan Xiao<sup>b</sup>, Yangqin Gao<sup>b</sup>, Ning Li<sup>a</sup>, Weiyu Song<sup>a</sup>, Lei Ge<sup>a,b,\*</sup>, Jian Liu<sup>a,\*</sup>

<sup>a</sup> State Key Laboratory of Heavy Oil Processing, College of New Energy and Materials, China University of Petroleum Beijing, No. 18 Fuxue Rd., Beijing, 102249, People's Republic of China

<sup>b</sup> Department of Materials Science and Engineering, College of New Energy and Materials, China University of Petroleum Beijing, No. 18 Fuxue Rd., Beijing, 102249, People's Republic of China

## ARTICLE INFO

### Keywords:

Photocatalysis  
Ni-Co Layered double hydroxides  
P-Doping CdS  
DFT Calculations

## ABSTRACT

Designing durable and highly active photocatalysts for hydrogen evolution via water splitting is still very challenging. Novel NiCo-LDH/P-CdS hybrid photocatalysts are fabricated by combining strategies of P-doping and in-situ loading of NiCo-LDH. P-doping creates a mid-gap at the bottom of the conduction band of CdS, which facilitates to prolong the life-time of the photo-induced electrons. Subsequently, the in-situ loading of NiCo-LDH is able to form heterojunctions between NiCo-LDH and P-CdS that not only promote the separation efficiency of carriers, but also effectively reduce the light corrosion phenomenon commonly observed in CdS. The as-prepared 2 mol% NiCo-LDH/40 wt% P-CdS sample shows a high visible-light catalytic H<sub>2</sub> production rate of 8.665 mmol·h<sup>-1</sup>·g<sup>-1</sup>, which is 45 times higher than pure CdS. The apparent quantum yield is determined to be 14.0% at 420 nm monochromatic light. Based on the calculation of density function theory (DFT), the rational photocatalytic mechanism has been proposed and is well consistent with the experimental results. Our study not only demonstrates a facile, eco-friendly and scalable strategy to synthesize highly efficient photocatalysts, but also provides a new viewpoint of the rational design and synthesis of advanced photocatalysts by harnessing the strong synergistic effects through simultaneously tuning and optimizing the electronic structure and surface.

## 1. Introduction

Renewable H<sub>2</sub> production from water splitting has been considered as an effective way to address the energy shortage and environmental issues. [1] Photocatalytic water splitting for hydrogen release using visible light or sunlight is an alternative strategy to boost the large-scale application of hydrogen energy. Among the semiconductors used for photocatalytic water splitting, such as carbon nitride [2,3], CeO<sub>2</sub> [4], TiO<sub>2</sub> [5–7], etc. CdS has been considered as one of the most efficient photocatalysts due to its suitable band gap and appropriate band position, and a tremendous amount of exploration on the photocatalytic performance of CdS have been carried out. [8–10] However, it is still a great challenge for photocatalytic materials to have high-efficiency and stability at the same time. On one hand, modifying CdS with co-

catalysts is considered as the most common method to improve its photocatalytic hydrogen evolution (PHE) efficiency [11–15]. On the other hand, appropriate elemental doping is considered as another important strategy to boost the performance of CdS by engineering its electronic structure. Elemental doping has been demonstrated to play a significant role in decreasing the band gap, enlarging the range of light absorption, boosting the efficiency of charge transfer and producing more active sites [16–19].

Elemental phosphorus, as an amphoteric impurity has been widely used to dope into the semiconductors to moderate the free energy of H<sub>2</sub> adsorption, changing the type of minority charge carriers and carrier density of the semiconductors. [20,21] This approach has also been applied in the field of photocatalysis for water splitting. Very recently, Huang et al has reported that doping P in the lattice of CdS can generate

\* Corresponding authors at: State Key Laboratory of Heavy Oil Processing, China University of Petroleum Beijing, No. 18 Fuxue Road, Beijing, 102249, People's Republic of China.

E-mail addresses: [gelei08@sina.com](mailto:gelei08@sina.com) (L. Ge), [liujian@cup.edu.cn](mailto:liujian@cup.edu.cn) (J. Liu).

<sup>1</sup> S.S.L. and L.W. contributed equally.

<https://doi.org/10.1016/j.apcatb.2019.05.001>

Received 16 February 2019; Received in revised form 22 April 2019; Accepted 1 May 2019

Available online 01 May 2019

0926-3373/© 2019 Elsevier B.V. All rights reserved.

an oriented built-in electric field for efficient extraction of charge carriers [22]. Before long, Chen's group fabricated  $\text{Zn}_x\text{Cd}_{1-x}\text{S}$  with P doping, and found that P doping can effectively elongate the lifetime of the charge carriers, not only the  $\text{H}_2$  generation performance was enhanced, but also the separation of photo-induced electrons was promoted. [23]

Layer structured semiconductors, such as layered perovskites, layered cationic clays and layered double hydroxides (LDH) have attracted much attention due to their high layer charge density along with two-dimensional interlayer spaces of height, which are available for generating a rational path for charge conveying. [24] Among these layer structured semiconductors, layered double hydroxides are brucite like solids that are constituted by two metal cations typically having  $2^+$  ( $\text{M}^{\text{II}}$ ) and  $3^+$  ( $\text{M}^{\text{III}}$ ) oxidation states, octahedrally surrounded by oxo bridges and hydroxyl groups. The primary structural feature of LDH materials is that the  $\text{M}^{\text{II}}$  and  $\text{M}^{\text{III}}$  cations are distributed uniformly in the hydroxide layers and the optimization of the electronic structure can be achieved by simply adjusting the chemical composition of the cations. [25,26] LDH materials have shown excellent activities in the field of photocatalysis because of their large surface area, high density of active sites, positively charged brucite-like layers, and exchangeable interlayer anions [27]. As for the structure of LDH, the  $\text{M}^{\text{III}}$  has partly replaced  $\text{M}^{\text{II}}$  in the lattice of  $\text{M}(\text{OH})_2$ , which is composed by sheets of edge-sharing  $\text{M}(\text{II})\text{O}_6$  and  $\text{M}(\text{III})\text{O}_6$  octahedral units. This structure has been reported that the high dispersion of transition metal octahedra has the merits of facilitating the electrons transfer and avoiding recombination of electrons and holes. [28,29] It is noted that many groups have reported LDHs such as: NiFe [30], ZnCr [27], CoAl-LDH [31] and NiAl-LDH [32] can act as co-catalysts in the field of water splitting for  $\text{O}_2$  and  $\text{H}_2$  releasing. [33,34] Zhang et al has designed modular catalysts Ni-MgO- $\text{Al}_2\text{O}_3$  via the template of NiMgAl-LDH and showed excellent coke- and wintering-resistance in the drying of methane reaction. [35] Kulamani et al [36] has reported that NiFe-LDH/g- $\text{C}_3\text{N}_4$  photocatalyst shows an excellent photocatalytic activity towards water oxidation and reduction reaction. Ebrahim's group has proved that NiCo-LDH owns repaid transfer of electrons and are efficient for opening the channels to release gaseous products. [37] These remarkable photocatalytic performances over LDH-based composites render these materials a rational platform for exploring novel and efficient photocatalysts.

Motivated from above studies, in this report we have coupled NiCo-LDH with P-doped CdS to form nanoscale heterojunction, which shows a greatly enhanced  $\text{H}_2$  production performance compare with pure CdS under visible light illumination. In specific, doping CdS with P can effectively elongate the lifetime of the charge carries by boosting the efficiency of charge separation and suppressing the recombination rate of photo-induced electrons and holes. After loading NiCo-LDH on the surface of P-CdS, the heterojunction has formed to further promote the photo-generated charges separation, and also to inhibit the photo-corrosion of CdS. This makes NiCo-LDH/P-CdS one of the most promising photocatalysts for hydrogen evolution via water splitting. In addition, we utilize DFT calculations to explore the transfer behavior of the charge carriers and the photocatalytic mechanism of the NiCo-LDH/P-CdS hybrids, which is well consistent with the experimental results.

## 2. Results and discussion

### 2.1. Characterization of NiCo–OH/P-CdS hybrid samples

Fig. 1(a) presents the X-ray diffraction (XRD) patterns of the obtained samples, the diffraction pattern of P-CdS samples with different doping ratio of P are closely similar to that shown in pristine CdS. However, the enlarged patterns inserted in Fig. 1 (a) reveal that the main diffraction peaks of P-CdS are slightly shifted towards a lower  $2\theta$ , which indicates the lattice parameters of the P-CdS are slightly larger than that in pristine CdS. [38] The lattice spacing of pristine CdS (101)

is 0.313 nm, while P-CdS is 0.328 nm as determined in HRTEM analysis, which is consistent with the result obtained in XRD characterization. The subtle change in the crystal structure for P-CdS has been unveiled by the calculation of the bond distances in the crystal models shown in Fig. S1. It reveals that P atom has replaced the site of S atom and shows a non-negligible incensement in lattice parameters (CdS:  $a = 8.274 \text{ \AA}$ ,  $b = 8.274 \text{ \AA}$ ,  $c = 13.429 \text{ \AA}$ ; P-CdS:  $a = 8.614 \text{ \AA}$ ,  $b = 8.614 \text{ \AA}$ ,  $c = 13.480 \text{ \AA}$ ). The results indicate that the spacing of the (101) crystal plane in CdS is enlarged from  $3.31 \text{ \AA}$  to  $3.44 \text{ \AA}$ , which attributes to the larger radius of P (110 ppm) atom than the replaced S (102 ppm) atom. Furthermore, the calculation result is well consistent with the lattice spacing result obtained in HRTEM analysis. One thing needs to notice is that the defects introduced by P doping can not be ignored.

After NiCo–OH was in situ loaded on the surfaces of P-CdS, no noticeable change in XRD pattern has been observed in P-CdS, indicates an unchanged crystal structure. The typical diffraction peaks of the NiCo–OH sample are located between the diffraction peaks of  $\beta\text{-Co}(\text{OH})_2$  (JCPDS No. 30-0443) and  $\beta\text{-Ni}(\text{OH})_2$  (JCPDS No. 14-0177) (Fig. 1(b)). The close peak positions for  $\beta\text{-Co}(\text{OH})_2$  and  $\beta\text{-Ni}(\text{OH})_2$  are due to the similarity in physical and chemical properties of Ni and Co atoms. [39] Therefore the diffraction peaks at  $33^\circ$ ,  $38.4^\circ$ ,  $51.8^\circ$ ,  $58.7^\circ$  and  $62.3^\circ$  are corresponding to the planes of (100), (101), (002), (102) and (110) of  $\beta$ -phase NiCo–OH [40].

Raman spectroscopy is also applied to investigate the structural modification of samples (Fig. 1(d)). Obviously, both CdS and P-CdS have two characteristic peaks. The peak at  $300.23 \text{ cm}^{-1}$  corresponds to the first-order longitudinal optical (1-LO) mode and the other peak at  $600.73 \text{ cm}^{-1}$  corresponds to the 2-LO [41]. Moreover, the 1-LO and 2-LO peaks of P-CdS slightly redshift with respect to pristine CdS, which can be attributed to the lattice expansion along the c-axis as the peak value is reported to be very sensitive to the lattice strain along the c-axis [38].

NiCo-LDH/P-CdS hybrid system has been synthesized by three steps as illustrated in Scheme 1. Firstly, CdS is prepared through a simple solvothermal method. After that,  $\text{NaH}_2\text{PO}_2$  and CdS precursor are placed on both sides of the porcelain boat heating at  $300^\circ\text{C}$  for 1 h under Ar atmosphere. Phosphine ( $\text{PH}_3$ ) gas decomposed from  $\text{NaH}_2\text{PO}_2$  at temperature above  $200^\circ\text{C}$  acts as the source of P dopants. The actual doping amount of P are listed in Table 1 according to the detection of ICP-OES technique. Finally, NiCo-LDH is loaded on the surface of P-CdS by hydrothermal method (Scheme 1(b)).

The morphology and micro-structure of the obtained samples were characterized by TEM and SEM. Fig. 2(a) shows that the morphology of CdS is nanorods with the size of ca. 50–100 nm. The lattice distance is 0.313 nm shown in Fig. 2 (b) corresponding to the (101) plane of CdS. The crystal structure a006Ed morphology of CdS have no obvious changes after P doping. However, the lattice distance (0.328 nm) of P-CdS shown in Fig. 2(c) is larger than pure CdS, indicating that P has been successfully doped into the lattice of CdS. The two different lattice stripes (0.326 nm and 0.236 nm) shown in Fig. 2(d) are assigned to P-CdS and NiCo-LDH, respectively. The field-emission scanning electron microscopy (FE-SEM) images of NiCo-LDH are displayed in Fig. S2 (a) and (b), lamellar NiCo-LDH with a diameter of around 500 nm are found. In addition, the detailed structure of NiCo-LDH inserted in Fig S2 (b) exhibits that layer-by-layer ordered NiCo-LDH nanosheets are formed by self-assembly. However, NiCo-LDH is only loaded on the surface of P-CdS because the lattice stripes of P-CdS has not been changed. The elemental mapping shown in Fig. 2(e) clearly displays a well-defined spatial distribution of P, Ni, Co and O elements on the surface of CdS, which is beneficial for accelerating the rate of interface redox reactions.

XPS technique has been applied to gain further insight of the surface composition of CdS, 40 wt% P-CdS and 2 mol% NiCo-LDH/40 wt% P-CdS photocatalysts. Fig. 3(a), and (b) display the high-resolution spectra of Cd 3d and S 2p over the sample of pristine CdS and 40 wt% P-CdS. As for pure CdS, the binding energies at 404.7 eV and 411.4 eV are

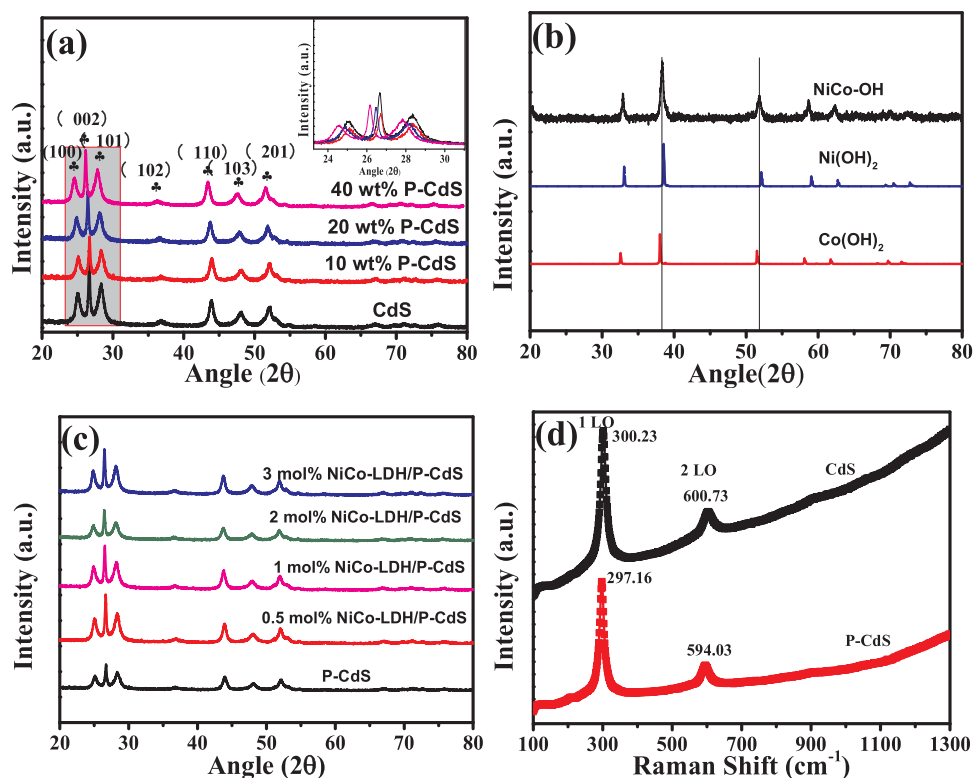
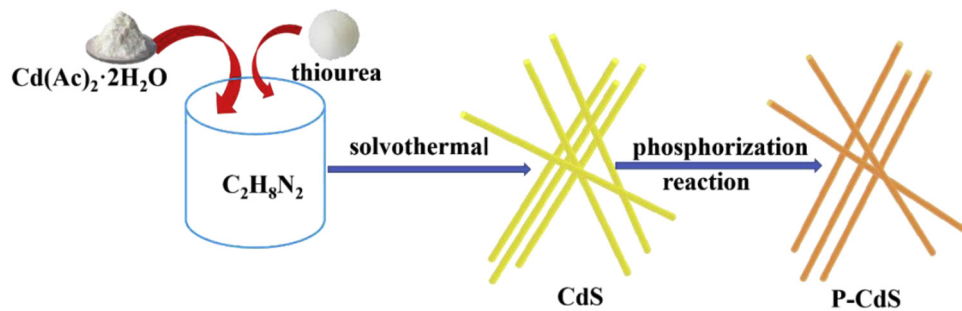


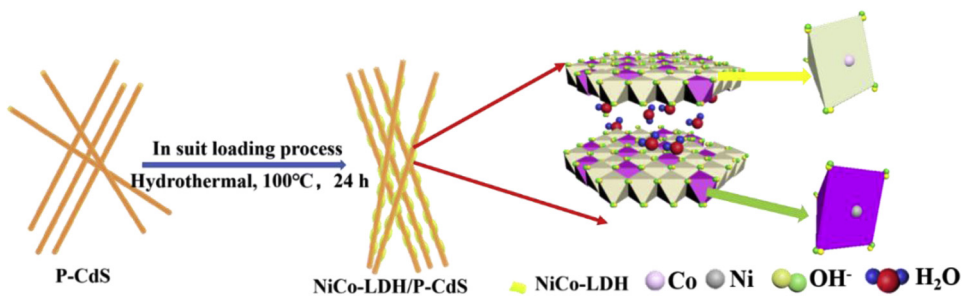
**Fig. 1.** XRD patterns of (a) CdS and P-CdS. The insert is the enlarge pattern range from 21.5° to 32.5° of CdS and P-CdS, (b) NiCo-LDH, (c) different loading amount of NiCo-LDH in P-CdS. (d) Raman shifts of CdS and P-CdS at 633 nm.

assigned to the characteristic peaks of Cd 3d<sub>3/2</sub> and Cd 3d<sub>5/2</sub>, respectively. The difference in binding energies for Cd 3d<sub>3/2</sub> and Cd 3d<sub>5/2</sub> is 6.7 eV, which indicates the existence of Cd<sup>2+</sup> on the surface of CdS. The spectra of Cd 3d couples with 161.2 eV and 162.4 eV for S 2p<sub>3/2</sub> and S 2p<sub>1/2</sub>, which are typical characters of CdS. [22] After doped P in the lattice of CdS, the Cd 3d and S 2p in 40 wt% P-CdS hybrids shift

positively compare to pristine CdS, which indicates that a fraction of P atoms has substituted S sites to form Cd-P bonds [23]. As shown in Fig. 3(c), three peaks around 129.5 eV, 130.4 eV and 133.6 eV can be indexed to CdP<sub>2</sub>, [42] P 2p<sub>1/2</sub> and oxidized phosphorous which formed during exposure to air or synthesis process. The Co 2p spectra are illustrated in Fig. 3(d), two evident peaks at 780.7 eV and 796.6 eV are



**a.** Synthesis route of CdS and P-CdS



**b.** Synthesis route of NiCo-LDH/P-CdS.

**Scheme 1.** Schematic illustration of the synthetic process of hierarchical NiCo-LDH/P-CdS.



**Table 1**

Real value for the amount of P obtained by inductively coupled plasma atomic emission spectrometry (ICP-OES).

Samples	Real P content
10 wt% P-CdS	0.9 wt%
20 wt% P-CdS	1 wt%
30 wt% P-CdS	1.8 wt%
40 wt% P-CdS	2.8 wt%
50 wt% P-CdS	3.3 wt%

assigned to Co 2p<sub>3/2</sub> and Co 2p<sub>1/2</sub> orbitals, respectively. The other two satellite peaks around 778 eV and 793.2 eV denote to “Sat.” in the Co 2p spectra. In addition, the Co 2p spectrum can be best fitted with two spin-orbit doublets by employing Gaussian fitting method, and the peaks are well consistent with the positions of both the Co<sup>2+</sup> and Co<sup>3+</sup>. [43–45] The analogous two spin-orbit doublets characteristic of Ni<sup>2+</sup> and Ni<sup>3+</sup> with two shakeup satellites also exist in the spectrum of Ni 2p (Fig. 3(e)). As for O 1s spectrum, three peaks approximately located at 530.8 eV, 531.1 eV and 533.8 eV are corresponded to O-Ni bond, O-Co bond and physis- and chemisorbed water. [46] However, the binding energies value of Ni 2p and Co 2p in the sample of 2 mol% NiCo-LDH/40 wt% P-CdS are all shifted negatively than pure NiCo hydroxide reported precedingly [47]. This strongly manifests that there are intimate interfaces formed between NiCo-LDH and P-CdS, which are favorable for fast charge separation and conveying.

The light absorption property of all samples is explored by UV–vis absorption spectra as displayed in Fig. 4(a). The absorption edge of pure CdS appears at 561 nm. After doped P in the lattice of CdS, it is notably that an evident enhancement in absorption can be observed in the region from 500 nm to 700 nm. This significant enhancement in the optical absorption can be attributed to the narrowed band gap. Doping of P reduces the band gap of the catalyst and the result is displayed in the insert image. The band gap of the semiconductor can be determined by considering the following relation:

$$(ah\nu)^{\frac{1}{n}} = A(h\nu - E_g) \quad (1)$$

Where  $\alpha$ ,  $h$ ,  $\nu$ ,  $A$  and  $E_g$  are present as absorption coefficient, Planck's constant, light frequency, a constant and band gap energy, respectively. Moreover, the value of  $n$  is determined by the type of optical transition of the semiconductor, where  $n = 1/2$  is for direct transition and  $n = 2$  for indirect transition. According to the DFT calculations, the variation in the band structures of CdS and P-CdS are shown in Fig. 5 (a) and (b). For the band structure diagrams, the  $k$ -points path  $\Gamma$ -M-K- $\Gamma$ -A-L-H-A is presented in detail. [46] It can be seen that both pure CdS and P-CdS are direct band gap semiconductors, in which the valence band maximum and conduction band minimum of the two catalysts are located at the same  $k$ -point. Therefore, in this case, the value of  $n$  in Eq. (1) is 1/2. The band gap of pristine CdS and P-CdS is 2.21 eV and 2.08 eV, respectively. Obviously, the sample of P-CdS in this work shows a considerable tail absorption (Urbach tail) in the visible light region, where the Urbach tail is ascribed to the electronic states located within the band gap (usually regard as mid-gap states), indicating an increased

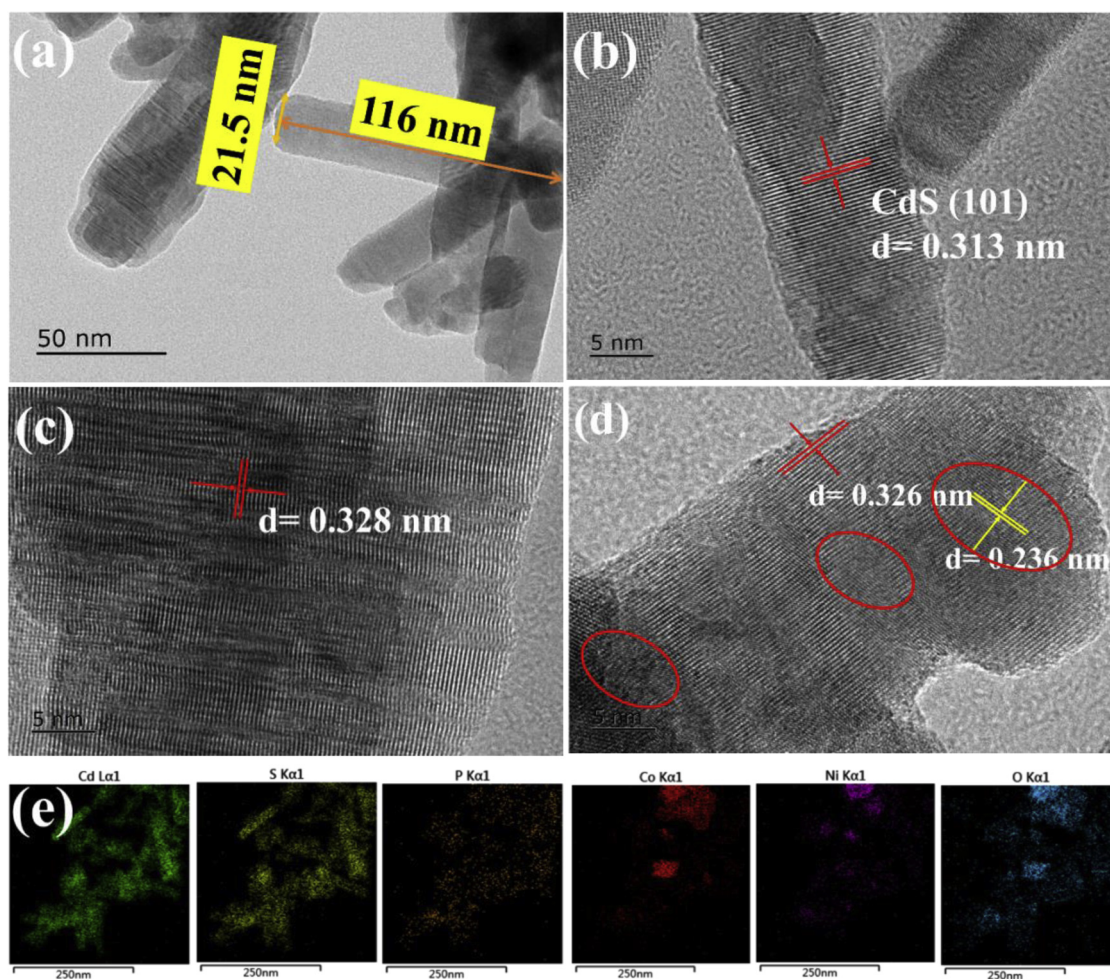


**Fig. 2.** TEM images of (a) CdS nanorods (b) HRTEM of CdS (c) HRTEM of P-CdS (d) HRTEM of NiCo-LDH/P-CdS (e) Mapping of Cd, S, Co, Ni, P and O in sample of NiCo-LDH/P-CdS.

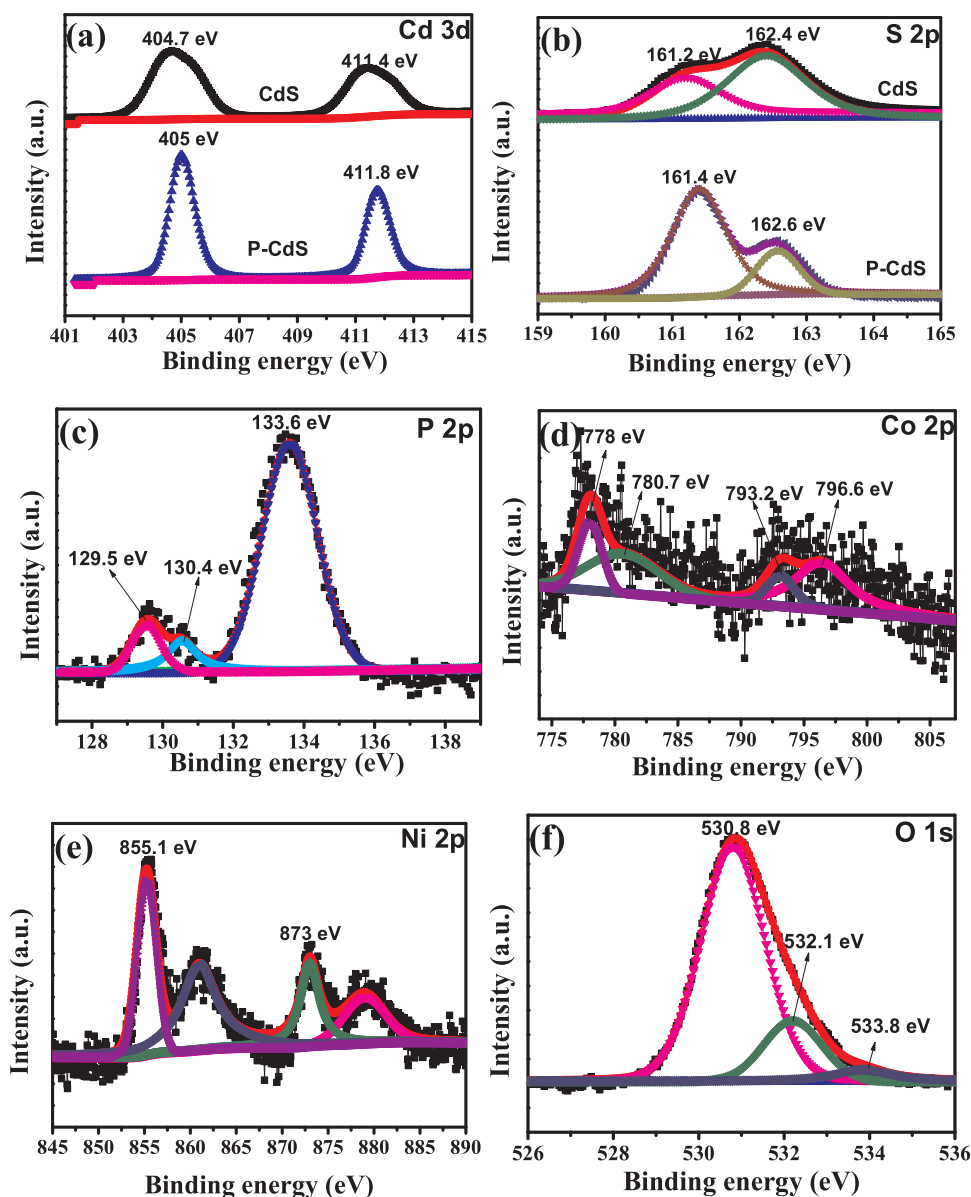


Fig. 3. High resolution XPS spectra of (a) Cd 3d, (b) S 2p, (c) P 2p, (d) Co 2p, (e) Ni 2p, (f) O 1s over the sample of NiCo-LDH/P-CdS.

doping defect in P-CdS. [48–50] In order to verify the reason of the mid-gap states, the partial density of state (PDOS) of CdS and P-CdS were calculated by DFT studies. However, the description of exchange-correlation effects utilizes the general gradient approximation (GGA), which always leads to an under estimation of band gaps for transition metals resulting in difference as compared with the experimental result [51,52]. The result displays that after P doping the intrinsic band gap of CdS is narrowed from 0.76 eV to 0.66 eV (Fig. 6(a) and (b)). In addition, the empty mid-gap states origins from the hybridization of P 3s3p and Cd 4s3d appear below the conduction band of CdS. According to previous studies, the empty mid-gap states can act as electron sinks that accommodates photo-induced electrons from the valence band of P-CdS, in this case, it will absorb photons with lower photon energies than the band gap of pure CdS, thus leading to the arising of Urbach tail light absorption. [53,54]

Basing on the result of XRD and TEM, loading NiCo-LDH does not change the crystal structure of P-CdS, the change in visible light absorption can be verified by the color change in the x mol % NiCo-LDH/40 wt% P-CdS, which is changed from earthy orange to shallow orange after NiCo-LDH loaded on the surface of P-CdS. However, this type of

light absorption variation could not be available for excitation of photocatalysts to generate photo-induced charges separations. [22] Fig. 4(b) displays the UV–vis absorption spectrum of NiCo-LDH, which indicates that the band gap of NiCo-LDH is 2.2 eV and has great potential to further generate photo-induced electron-hole pairs.

The semiconductor type and conduction band position of the samples are characterized by Mott-Schottky (M–S) plots at frequency of 1.0 KHz in 0.5 M Na<sub>2</sub>SO<sub>4</sub> solution. As displays in Fig. 4(c), CdS, 40 wt% P-CdS and NiCo-LDH all show a positive slope in M–S plots, which means that they exhibit n-type semiconductor properties. [55,56] The flat band position ( $V_{fb}$ ) of CdS and NiCo-LDH are measured to be -0.52 V and -0.69 V vs. RHE, respectively. Compare with pure CdS, the  $V_{fb}$  of P-CdS is positively shifted to -0.49 V vs. RHE. Then the transition energy from valance band position to mid-gap as for P-CdS is estimated to be 1.88 eV in Fig. 4(a). As a result that the exact position of mid-gap states of P-CdS is determined to be -0.49 V vs. RHE. Theoretically, the conduction band position of n-type semiconductors is -0.2 V negative than flat band potential. [57] So the conduction band positions of CdS, P-CdS and NiCo-LDH are -0.72, -0.69 and -0.89 V vs. RHE. Therefore, after doped P in the lattice of CdS, the  $E_{CB}$  of P-CdS is almost equal to pristine

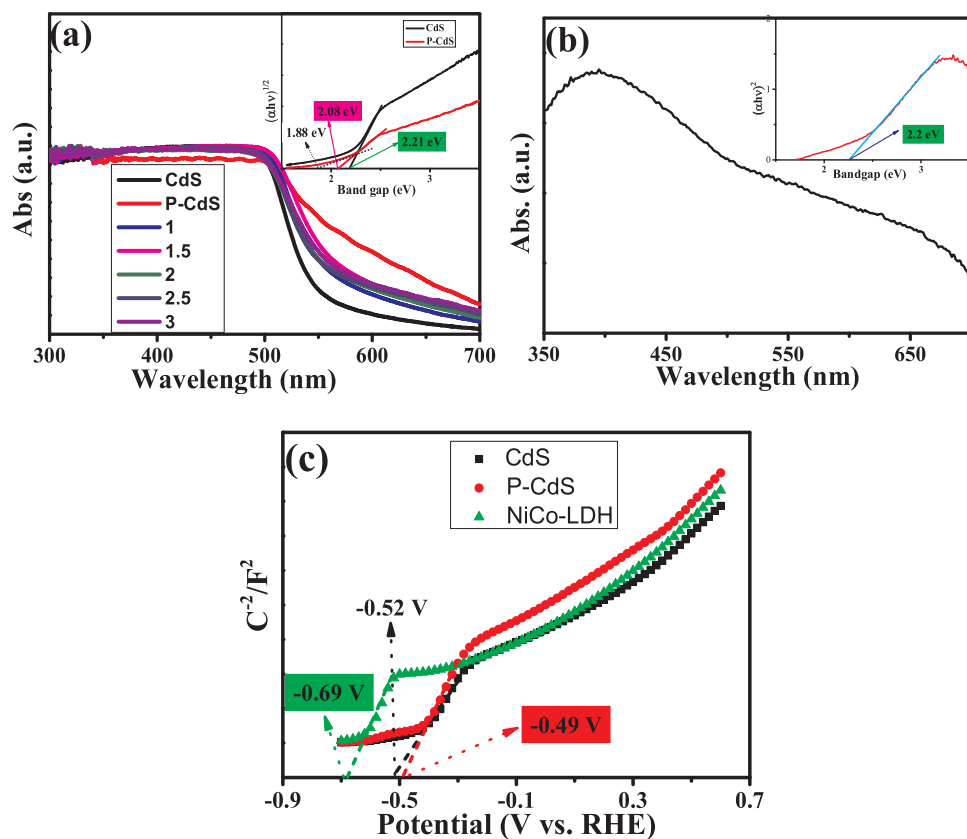


**Fig. 4.** (a) UV-vis absorption spectra over the samples of CdS, 40 wt% P-CdS and x mol% NiCo-LDH/P-CdS (x = 1, 1.5, 2, 2.5, 3), the inset is CdS and 40 wt% P-CdS band gap evaluation from the plot of  $(\alpha h\nu)^{1/2}$  vs. the absorbed photon energy ( $h\nu$ ). (b) UV-vis absorption spectra of NiCo-LDH and inset is band gap plot, (c) Mott-Schottky plots of CdS, 40 wt% P-CdS and NiCo-LDH at frequency 1.0 kHz in 0.1 M  $\text{Na}_2\text{SO}_4$  solution.

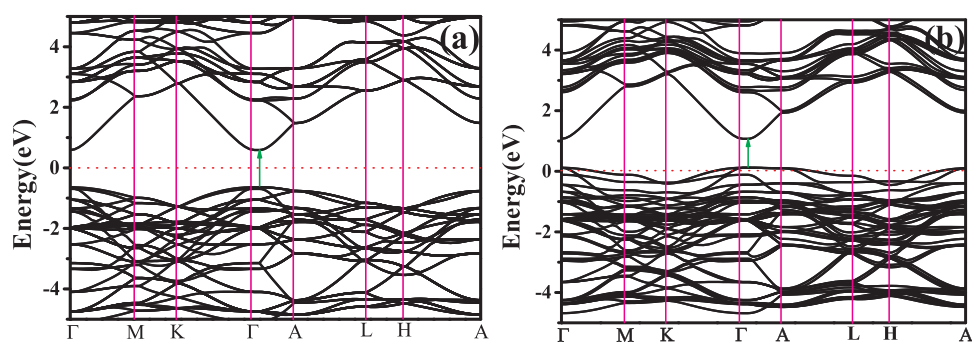


**Fig. 5.** Band structures of (a) CdS and (b) CdS-P.

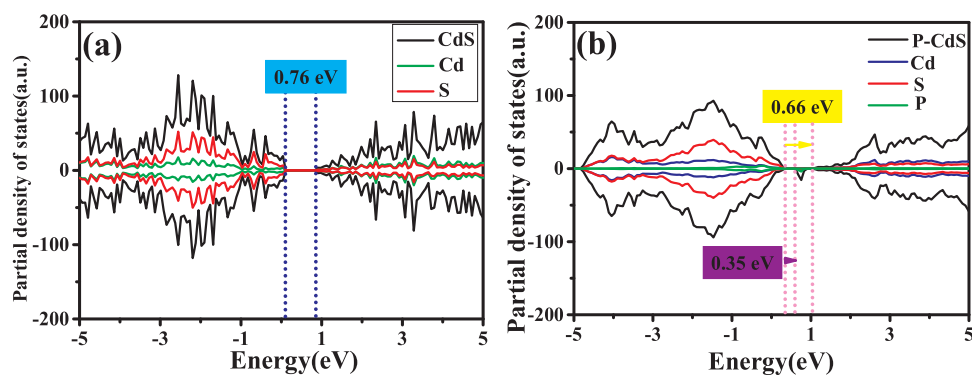


**Fig. 6.** Density of state distributions of (a) CdS and (b) CdS-P.

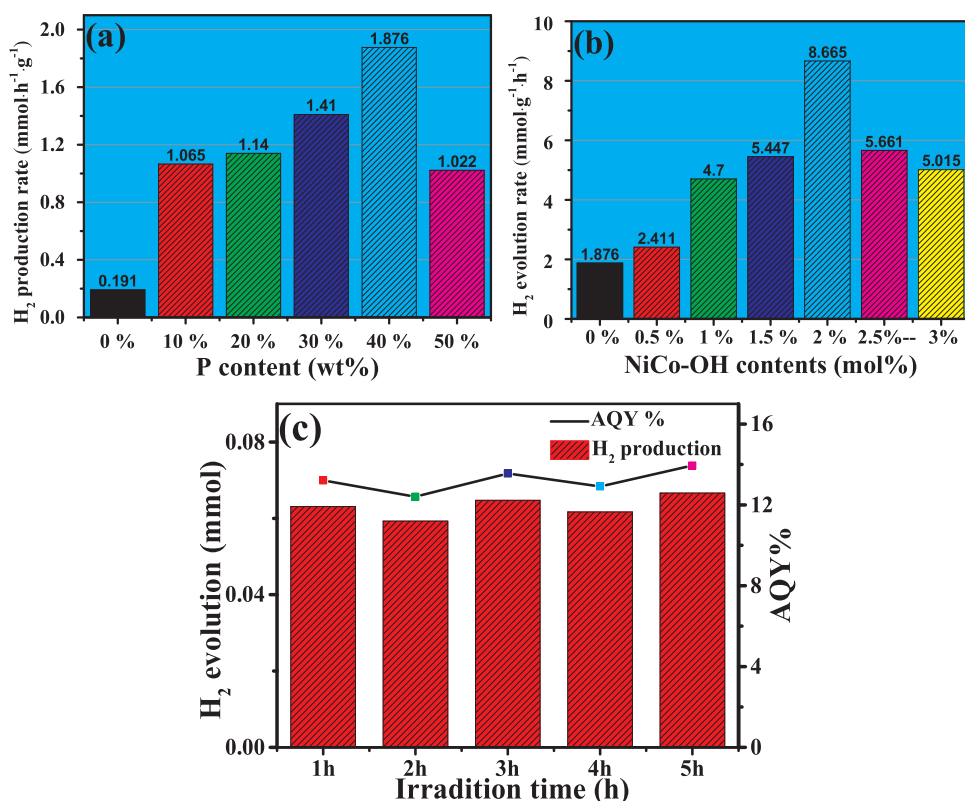


**Fig. 7.** (a) Rate of H<sub>2</sub> evolution over samples of x wt% P-CdS (x = 0, 10, 20, 30, 40, 50). (b) Rate of H<sub>2</sub> evolution over x mol% NiCo-LDH/40 wt% P-CdS composite samples with different NiCo-LDH contents. (c) H<sub>2</sub> production and quantum efficiency over the sample of 2 mol% NiCo-LDH/40 wt% P-CdS under 420 nm light irradiation.

CdS. However, the band gap ( $E_g$ ) of P-CdS is narrowed by 0.13 eV as compared with CdS, it can be concluded that the valance band position ( $E_{VB}$ ) is raised about 0.1 eV, correspondingly.

## 2.2. Photocatalytic H<sub>2</sub> evolution activity

The photocatalytic activities of the samples are characterized by H<sub>2</sub> production from an aqueous solution composed of 90 ml H<sub>2</sub>O and 10 ml lactic acid as scavengers under visible light irradiation. As shown in Fig. 7(a), the HER rate (0.191 mmol·h<sup>-1</sup>·g<sup>-1</sup>) of pure CdS under visible light irradiation is negligible. However, after y wt% P is doped into the CdS sample, all of specimens exhibit relatively high photocatalytic activities under the same characterization conditions as adopted before. The sample of 40 wt% P-CdS shows the highest H<sub>2</sub> production activity of 1.876 mmol·h<sup>-1</sup>·g<sup>-1</sup>, which is approximately 9.8 folds higher than pure CdS. NiCo-LDH is a promising co-catalyst in the field of water splitting for H<sub>2</sub> production, and the band position of NiCo-LDH is suitable for P-CdS to construct II-type heterojunction. When a certain amount of NiCo-OH co-catalyst has been loaded on the surface of the 40 wt% CdS-P, the H<sub>2</sub> evolution activity is improved significantly. Fig. 7(b) presents the H<sub>2</sub> evolution rate over NiCo-LDH/P-CdS samples with different NiCo-LDH contents. After loading 2 mol% NiCo-LDH on P-CdS, the H<sub>2</sub> evolution activity is remarkably increased to 8.665 mmol·h<sup>-1</sup>·g<sup>-1</sup>, which is 4.6 folds higher of 40 wt% P-CdS and 45 folds higher of pure CdS. The apparent quantum efficiency of 2 wt% NiCo-LDH/P-CdS at 420 nm reaches the highest value of 14%, in which the monochromatic light source was obtained by 300 W Xe lamp equipped with a 420 nm (± 5 nm) band pass filter, the characterization

is lasted for a total duration of 5 h and the result is listed in Table 2. The specific calculation details of apparent quantum efficiency (AQE%) according to Eq. S (1) are presented in supporting information. However, the H<sub>2</sub> production rate then starts to decrease when further increasing the NiCo-LDH content, which can be attributed to the excess co-catalysts has sheltered the active sites of P-CdS. Moreover, the interfaces and heterojunction structures formed between NiCo-LDH and P-CdS has decreased with excess content of NiCo-LDH, which results in suppressed charges transfer efficiency and photocatalytic activity. [58]

Furthermore, the stability of 2 mol% NiCo-LDH/40 wt% P-CdS has been checked and the result is displayed in Fig. 8(a). It can be seen that the photocatalyst exhibits excellent stability after 4 cycles (16 h), which means that this heterostructure system can effectively reduce photo-corrosion and promote the stability of CdS. We have characterized the Cd<sup>2+</sup> concentration in the test solution using ICP-OES method for samples of pure CdS, 40 wt% P-CdS and 2 mol% NiCo-LDH/40 wt%P-CdS, before and after photocatalytic activities characterizations. Notably, Fig. 8(b) displays that the Cd<sup>2+</sup> concentration of pure CdS after 4 h photocatalytic experiment is significantly increased as compared with that before the stability characterization, which means that photo-corrosion is quite serious during the photocatalytic process of CdS [59]. However, there is only negligible Cd<sup>2+</sup> in the system of NiCo-LDH/P-CdS. In addition, Our group have also summarized some CdS-based photocatalysts for hydrogen evolution reaction under different light range irradiation in table S1. It proves that the system of NiCo-LDH/P-CdS not only has great photocatalytic activity, but also shows excellent stabilities. The specific mechanism will be discussed at length in the later part of photocatalytic mechanism.

**Table 2**

AQY% of 2 mol% NiCo-LDH/40 wt %P-CdS sample irradiation for 5 h.

	1h	2h	3h	4h	5h
AQY %	13.2	12.4	13.6	12.9	14
light intensity (mW/cm <sup>2</sup> )	3.8	3.8	3.4	3.3	3.8

## 2.3. Charge-carrier separation and transport

The combined techniques of steady-state PL and TRPL spectroscopy, as well as electrochemical impedance spectroscopy (EIS) are employed to investigate the charge separation and transfer behaviors in the hybrid system of NiCo-LDH/P-CdS. Normal temperature PL spectra of



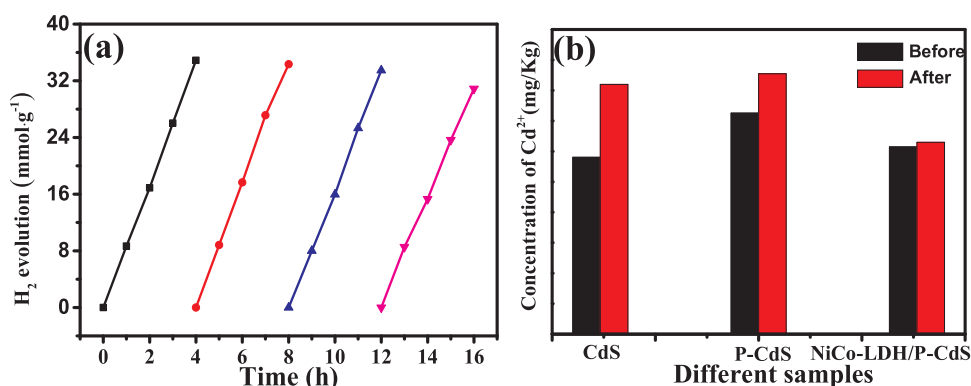


**Fig. 8.** (a) Stability tests of hydrogen evolution over the sample of 2 mol% NiCo-LDH/40 wt% P-CdS, (b) The concentration of Cd<sup>2+</sup> for each sample of CdS, 40 wt% P-CdS and 2 mol% NiCo-LDH/40 wt %P-CdS before and after photocatalytic activity under visible light irradiation.

samples are showed in Fig. 9(a) with an excitation wavelength of 400 nm. Comparing with pure CdS, the P-CdS shows a lower PL peak intensity, suggesting that the photocatalyst displays a suppressed charge recombination of the photogenerated carriers, this may be caused by the enhanced charge diffusion rate in the P-CdS system raised from P doping. The result also further confirms that the mid-gap state induced by P-doping behaves as charge-carrier traps, which can impede electron-hole recombination instead of acting as a recombination center. [60,61] Among these samples, the PL signal of P-CdS becomes significantly quenched after subsequent loading NiCo-LDH on the surface, indicating that the charge recombination is further suppressed. The quenching effect is due to the synergistic behavior of both NiCo-LDH and P-CdS, causing an easy transfer of electrons from NiCo-LDH to P-CdS and holes migrate from P-CdS to NiCo-LDH.

Charge carrier lifetime is an important factor to determine the probability of photogenerated charge carriers in participating in the photocatalytic activity before recombination. [62,63] Usually, the longer carrier lifetime indicates the higher possibility of their participation in the photocatalytic reactions, thus the time-resolved photoluminescence (TRPL) characterization is investigated and shown in Fig. S3. Compare with pure CdS, P-doped CdS and NiCo-LDH/P-CdS show longer lifetimes. In contrast, after doping P in the lattice of CdS, the lifetime of charge carriers is extended from 0.9646 ns to 1.1514 ns (Fig. S3 (a) and (b)). Because of the existence of mid-gap states, the photogenerated carriers can be first captured by the trap states. Then the trapped charges can be re-excited to the conduction band and reach a dynamic equilibrium, so that can prolong the life time of electrons. Subsequently, the loading NiCo-LDH has further improve the lifetime

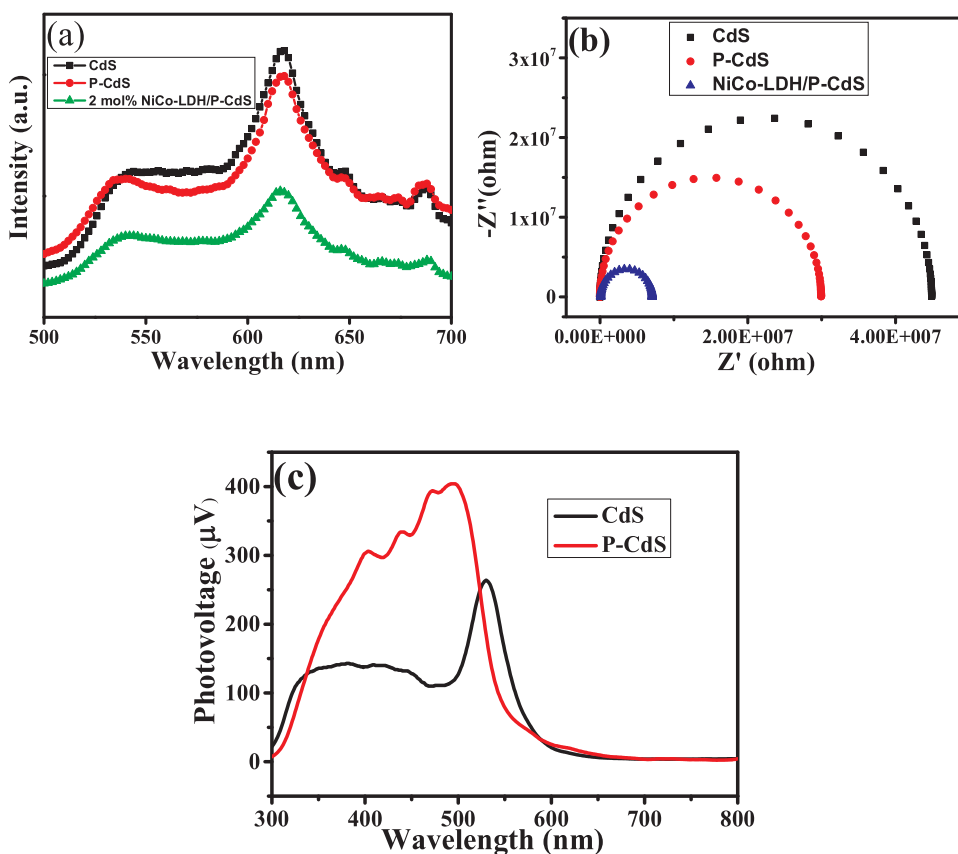


**Fig. 9.** (a) Room-temperature PL spectra, (b) electrochemical impedance spectroscopy (EIS) Nyquist plots of CdS, 40 wt% CdS-P and 2 mol% NiCo-LDH/40 wt% CdS-P, (c) SPV spectra of CdS and P-CdS.



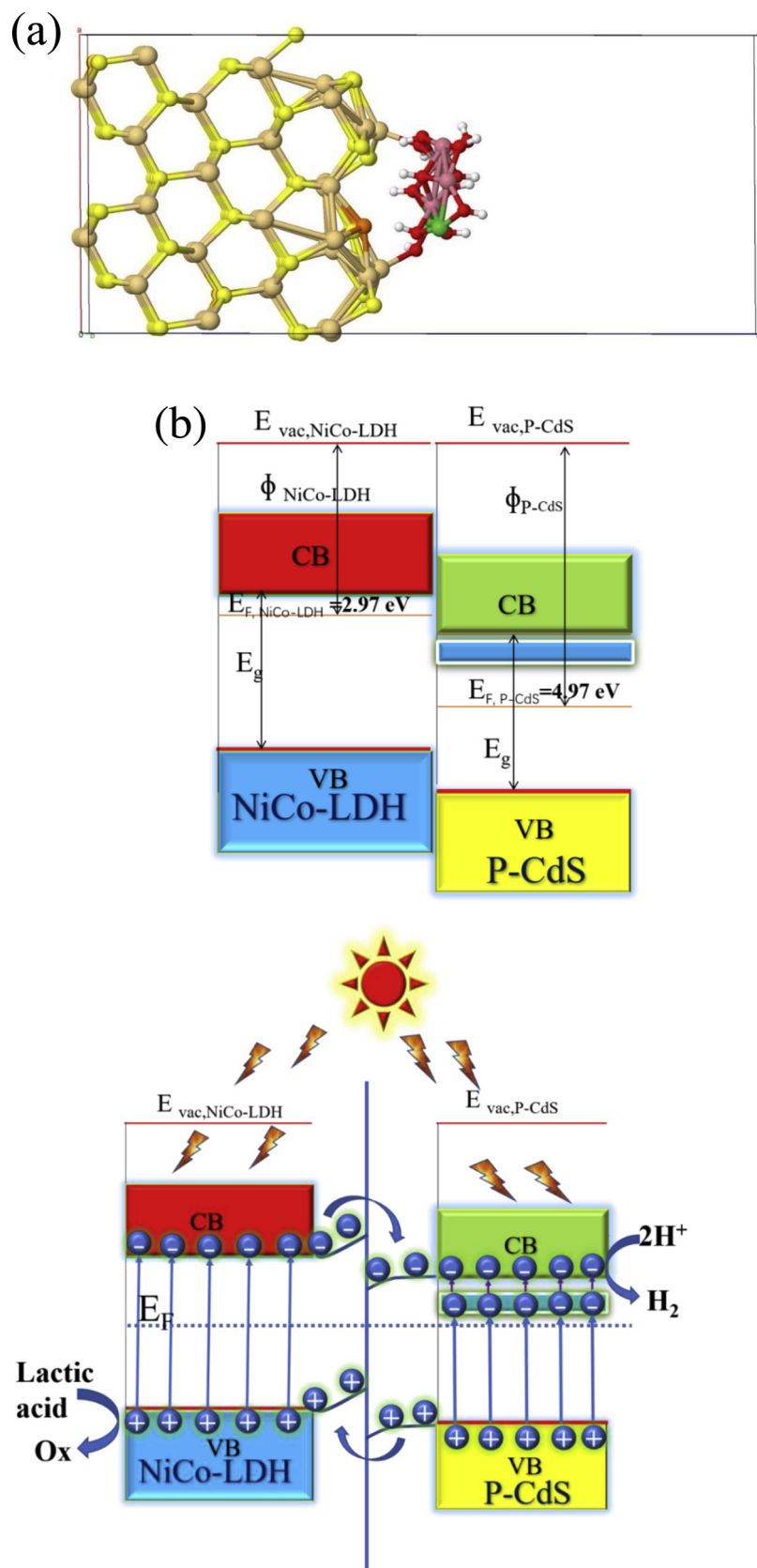


**Fig. 10.** Schematic of photocatalysis by NiCo-LDH/P-CdS composites. (a) The illustration of combination between NiCo-LDH (Co: green, Ni: pink, O: red, H: white) and semiconductor P-CdS (Cd atom is brown; the S atom is yellow; and the P atom is orange). (b) Calculated work function and band bending of NiCo-LDH and P-CdS (For interpretation of the references to colour in this figure legend, the reader is referred to the web version of this article).

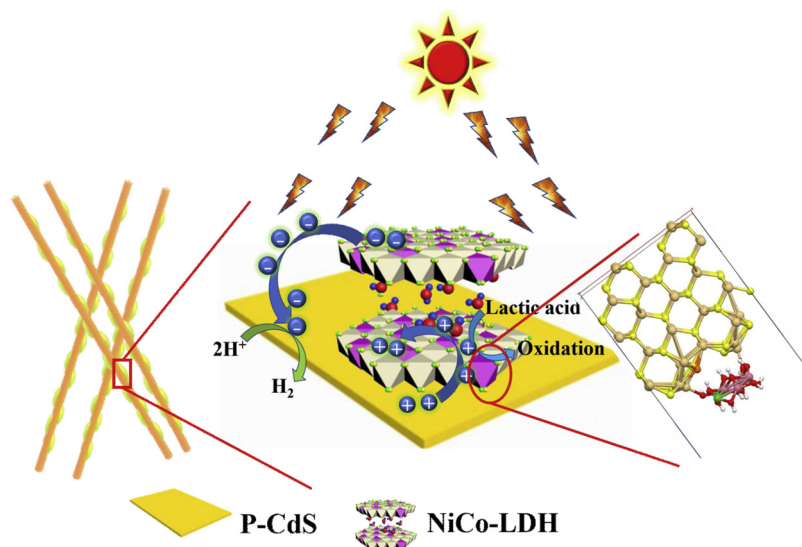


Fig. 11. Schematic illustration of charge transfer and  $\text{H}_2$  evolution mechanism of NiCo-LDH/P-CdS under visible light irradiation.

( $\tau = 1.1960$  ns) of electrons. This effect is attributed to the formation of a typical type-II band alignment structure between P-CdS and NiCo-LDH, facilitating the separation and transfer of photo-induced charges.

SPV is a functional technique to prove the validity mechanism and investigate the efficiency of charges separation above, which is presented in Fig. 9(c). In theory, the stronger photoelectric signal represents the higher photoinduced charge separation efficiency. The pristine CdS shows weaker response compares with P doped CdS because of poor separation and rapid recombination of photo-induced electron-hole pairs. However, the signal is much stronger after doped P into the lattice of CdS, which indicates that P doped can boost the separation and transmission efficiency of electron-hole pairs. The SPV spectra couples with the consequence of the above tests and analysis indicate that the mid-gap formed in CdS plays a significant role in charges separations and life extension.

PL, TRPL and SPV technique provide evidence to explore the separation and transfer efficiency of photo-induced electron-hole pairs of the samples under illumination condition. The characterization of EIS (Fig. 9(b)) has been used to obtain a deep insight into the charge transfer behaviors of the samples under dark conditions. Among all samples, P-CdS shows the smaller diameter than pure CdS, suggesting that the lower resistance for interfacial charge transfer from electrode to electrolyte molecules. Notably, P-doping not only possesses the higher efficiency of charge separation, but also boosts the charge transfer to the reactant molecules absorbed on the surface active sites. Moreover, loading NiCo-LDH on the surface of P-CdS can further increase electrons density and charges transfer efficiency, which is consisted with the photocatalytic performance of the samples. Combined with the above analysis, therefore, the transfer and separation capability of photo-induced carries play an outstanding role in the enhanced photocatalytic activities.

#### 2.4. Photocatalytic mechanism discussion

It is well known that the photocatalytic hydrogen generation reaction mechanism including four consecutive steps: a) the appropriate band gap to absorb light; b) forming electron-hole pairs under light irradiation; c) charges separation and transfer to the surface of photocatalysts; d) surface absorbed and occur redox reactions. [64,65] The four necessary steps are closely related to the electron density, surface free energy and textural structures of the material. Thus, optimal photocatalytic hydrogen production can be achieved if all the factors can be well regulated [66].

In this system, P-doping introduces the mid-gap states and results in changing of the electronic band structure of CdS in Figs. 5 and 6. The mid-gap states not only can extend the region of visible-light absorption, but also can act as the separation centers to temporarily trap photo-induced electrons excited from the VB of CdS, and then transfer to the CB of CdS, resulting in a prolonged lifetime of electrons. In addition, the HER pathway can be divided into three-state diagram, which is composed of (I) the initial state ( $\text{H}^+ + \text{e}^-$ ), (II) the intermediate adsorbed  $\text{H}^*$  and the ultimate product ( $1/2 \text{H}_2$ ). [67] The Gibbs free energy of  $\text{H}^*$  ( $|\Delta G_{\text{H}^*}|$ ) is an essential indicator to measure the HER activity for various photocatalysts. Pt as the most desirable and highly active HER catalyst, the  $|\Delta G_{\text{H}^*}|$  presents the value of  $\Delta G_{\text{H}^*} \approx -0.09$  eV, which means that the most ideal value of  $|\Delta G_{\text{H}^*}|$  should be approximate to zero. [68] Therefore, we have adopted DFT studies to calculate the values of  $\Delta G_{\text{H}^*}$  for  $\text{H}^*$  adsorption on the surface of P-CdS and NiCo-LDH ( $\theta = 0.33$  and  $0.5$ ) as displayed in Fig. S4. The NiCo-LDH ( $\theta = 0.5$ ) exhibits a very large negative value of  $-1.29$  eV that indicates  $\text{H}^*$  shows a strong chemical adsorption on the surface of NiCo-LDH. Meanwhile, the calculated value of  $\Delta G_{\text{H}^*}$  for NiCo-LDH ( $\theta = 0.33$ ) is  $-0.56$  eV, suggesting that  $\text{H}^*$  also can be relatively firmly adsorbed on the surface of NiCo-LDH, which means that very strong  $\text{H}^*$  adsorption and hard product desorption. [69] However, P-CdS shows a near-zero value of  $|\Delta G_{\text{H}^*}| \approx 0.27$  eV, clearly indicating that P-CdS displays a remarkable HER activity from the aspect of thermodynamics.

In order to investigate the experimental mechanism theoretically, work function values of P-CdS and NiCo-LDH were calculated by DFT and the interface model was constructed on the CdS (101) and NiCo-LDH (001). In our model system, the original work function values of P-CdS ( $4.97$  eV) is higher than NiCo-LDH ( $2.97$  eV) as shown in Fig. 10 and Fig. S5. The heterojunction between P-CdS and NiCo-LDH is formed after two semiconductors are in intimate contact, and thermal equilibrium is established, which causes hot electrons transfer from NiCo-LDH to CdS. Meanwhile, the photo-induced holes still remain in NiCo-LDH near the interface of NiCo-LDH /P-CdS, where a space charge layer and inherent electric field is formed. And the CB and VB of NiCo-LDH are bent upward, P-CdS downward, respectively, until the Fermi level of NiCo-LDH and P-CdS are aligned and the final Fermi energy is  $4.79$  eV. On one hand, electrons are excited from the VB to CB of NiCo-LDH under the visible light irradiation ( $\lambda \geq 400$  nm), and migrate across the upward band bending to the CB of P-CdS because of the relative positive conduction band position of P-CdS ( $-0.69$  V vs. RHE) than NiCo-LDH ( $-0.89$  V vs. RHE), leaving the photo-induced holes in the VB of NiCo-LDH; On the other hand, the electrons also can be

excited from the VB of CdS under the visible light irradiation and transfer to the mid-gap states, and then transfer to the conduction band of P-CdS after absorbing photons with certain energies. At the same time, the photo-generated holes transfer from the VB of P-CdS ( $E_{VB} = 1.39$  V vs. RHE) to the VB of NiCo-LDH ( $E_{VB} = 1.31$  V vs. RHE), and then be scavenged by lactic acid. The photo-induced electrons accumulated on the CB of P-CdS reducing  $H^+$  to  $H_2$  as shown in Fig. 10 and Fig. 11. Therefore, due to the existence of mid-gap states in P-CdS and formation of heterojunction between P-CdS and NiCo-LDH, both of them can effectively promote the separation of photo-induced charges and the suppress light corrosion effect.

### 3. Conclusions

In summary, a novel strategy combining P-doping and in-situ loading NiCo-LDH to synthesize an efficient hybrid photocatalyst of NiCo-LDH/P-CdS has been proposed. The new photocatalysts display decent visible-light photocatalytic hydrogen evolution rate of  $8.665 \text{ mmol h}^{-1} \text{ g}^{-1}$  with an apparent quantum yield of 14% at 420 nm. Notably, the induced mid-gap states at the bottom of the conduction band of CdS can dramatically extend the life-time of photo-generated charges which is favorable for enhanced photocatalytic activity. Furthermore, the formed heterojunction formed between NiCo-LDH and P-CdS could further promote the separation of photo-induced carriers as well as reducing the photo-corrosion effect. By combining the first principle calculations and experimental methodology, we found that the favorable photocatalytic performance can attribute to the synergetic effect of P-doping induced charge separation and heterojunction triggered electrons transfer from NiCo-LDH to P-CdS. This study has provided a new viewpoint to design highly active noble metal-free photocatalysts for solar light-driven  $H_2$  production.

### 4. Notes

The authors declare no competing financial interest.

### Acknowledgments

This work was financially supported by the National Science Foundation of China (Grant No. 51572295, 21273285 and 21003157), Beijing Nova Program (Grant No. 2008B76), and Science Foundation of China University of Petroleum, Beijing (Grant No. KYJJ2012-06-20 and 2462016YXBS05).

### Appendix A. Supplementary data

Supplementary material related to this article can be found, in the online version, at doi:<https://doi.org/10.1016/j.apcatb.2019.05.001>.

### References

- [1] Z. Shao, T. Zeng, Y. He, D. Zhang, X. Pu, Chem. Eng. J. 359 (2019) 485–495.
- [2] Q. Zhu, B. Qiu, M. Du, M. Xing, J. Zhang, Ind. Eng. Chem. Res. 57 (2018) 8125–8130.
- [3] G. Li, J. Shi, G. Zhang, Y. Fang, M. Anpo, X. Wang, Res. Chem. Intermed. 43 (2017) 5137–5152.
- [4] D. You, B. Pan, Y. He, X. Wang, W. Su, Res. Chem. Intermed. 43 (2017) 5103–5112.
- [5] Z. Xi, C. Li, L. Zhang, M. Xing, J. Zhang, Int. J. Hydrogen Energy 39 (2014) 6345–6353.
- [6] L. Zhang, B. Tian, F. Chen, J. Zhang, Int. J. Hydrogen Energy 37 (2012) 17060–17067.
- [7] L. Zhang, Z. Xi, M. Xing, J. Zhang, Int. J. Hydrogen Energy 38 (2013) 9169–9177.
- [8] X.B. Meng, J.-L. Sheng, H.L. Tang, X.J. Sun, H. Dong, F.M. Zhang, Appl. Catal. B 244 (2019) 340–346.
- [9] K. Zhang, M. Fujitsuka, Y. Du, T. Majima, ACS Appl. Mater. Interfaces 10 (2018) 20458–20466.
- [10] S. Wang, B. Zhu, M. Liu, L. Zhang, J. Yu, M. Zhou, Appl. Catal. B 243 (2019) 19–26.
- [11] R. Chen, Z.H. Yan, X.J. Kong, L.S. Long, L.S. Zheng, Angew. Chemie Int. Ed. 57 (2018) 16796–16800.
- [12] D.W. Wakerley, K.H. Ly, N. Kornienko, K.L. Orchard, M.F. Kuehn, E. Reisner, Chem. Eur. J. 24 (2018) 18385–18388.
- [13] H.-Q. Xu, S. Yang, X. Ma, J. Huang, H.L. Jiang, ACS Catal. 8 (2018) 11615–11621.
- [14] Z. Ai, Y. Shao, B. Chang, B. Huang, Y. Wu, X. Hao, Appl. Catal. B 242 (2019) 202–208.
- [15] L. Wang, W. Wang, Y. Chen, L. Yao, X. Zhao, H. Shi, M. Cao, Y. Liang, ACS Appl. Mater. Interfaces 10 (2018) 11652–11662.
- [16] Z. Lin, X. Wang, Angew. Chemie Int. Ed. 52 (2013) 1735–1738.
- [17] G. Dong, K. Zhao, L. Zhang, Chem. Commun. 48 (2012) 6178–6180.
- [18] J. Li, B. Shen, Z. Hong, B. Lin, B. Gao, Y. Chen, Chem. Commun. 48 (2012) 12017–12019.
- [19] Y. Wang, Y. Di, M. Antonietti, H. Li, X. Chen, X. Wang, Chem. Mater. 22 (2010) 5119–5121.
- [20] X. Fang, J. Li, D. Zhao, D. Shen, B. Li, X. Wang, J. Phys. Chem. C 113 (2009) 21208–21212.
- [21] Y. Shi, B. Zhang, Chem. Soc. Rev. 45 (2016) 1529–1541.
- [22] H. Huang, B. Dai, W. Wang, C. Lu, J. Kou, Y. Ni, L. Wang, Z. Xu, Nano Lett. 17 (2017) 3803–3808.
- [23] H.F. Ye, R. Shi, X. Yang, W.-F. Fu, Y. Chen, Appl. Catal. B 233 (2018) 70–79.
- [24] X. Sun, S.K. Dey, J. Colloid Interface Sci. 458 (2015) 160–168.
- [25] K. Teramura, S. Iguchi, Y. Mizuno, T. Shishido, T. Tanaka, Angew. Chemie Int. Ed. 51 (2012) 8008–8011.
- [26] P.C.A. Alberius, K.L. Frindell, R.C. Hayward, E.J. Kramer, G.D. Stucky, B.F. Chmelka, Chem. Mater. 14 (2002) 3284–3294.
- [27] B. Luo, R. Song, D. Jing, Int. J. Hydrogen Energy 42 (2017) 23427–23436.
- [28] D. Won Hwang, J. Kim, T. Jin Park, J.S. Lee, Mg-Doped WO<sub>3</sub> as a Novel Photocatalyst for Visible Light-induced Water Splitting, (2002).
- [29] L. Mohapatra, D. Patra, K. Parida, S.J. Zaidi, Eur. J. Inorg. Chem. (2017) 723–733 2017.
- [30] R. Boppella, C.H. Choi, J. Moon, D. Ha Kim, Appl. Catal. B 239 (2018) 178–186.
- [31] P. Cai, S. Ci, N. Wu, Y. Hong, Z. Wen, Physica Status Solidi A Appl. Res. 214 (2017) 1600910.
- [32] S. Tonda, S. Kumar, M. Bhardwaj, P. Yadav, S. Ogale, ACS Appl. Mater. Interfaces 10 (2018) 2667–2678.
- [33] Y. Zhao, P. Chen, B. Zhang, D.S. Su, S. Zhang, L. Tian, J. Lu, Z. Li, X. Cao, B. Wang, M. Wei, D.G. Evans, X. Duan, Chem. Eur. J. 18 (2012) 11949–11958.
- [34] C.G. Silva, Y. Bouizi, V. Fornés, H. García, J. Am. Chem. Soc. 131 (2009) 13833–13839.
- [35] X. Du, D. Zhang, R. Gao, L. Huang, L. Shi, J. Zhang, Chem. Commun. 49 (2013) 6770–6772.
- [36] S. Nayak, L. Mohapatra, K. Parida, J. Mater. Chem. A 3 (2015) 18622–18635.
- [37] A. Pirkarami, S. Rasouli, E. Ghasemi, Appl. Catal. B 241 (2019) 28–40.
- [38] R. Shi, H.F. Ye, F. Liang, Z. Wang, K. Li, Y. Weng, Z. Lin, W.F. Fu, C.M. Che, Y. Chen, Adv. Mater. 30 (2018) 1705941.
- [39] G. Hongyi, G. Wang, M. Yang, L. Tan, J. Yu, Novel tunable hierarchical Ni–Co hydroxide and oxide assembled from two-wheeled units (2011).
- [40] D.S. Hall, D.J. Lockwood, C. Bock, B.R. MacDougall, Proc. Math. Phys. Eng. Sci. 471 (2015) 20140792–20140792.
- [41] L. Zeiri, I. Patla, S. Acharya, Y. Golan, S. Efrima, J. Phys. Chem. C 111 (2007) 11843–11848.
- [42] R. Franke, T. Chassé, P. Streubel, A. Meisel, J. Electron Spectros. Relat. Phenomena 56 (1991) 381–388.
- [43] C. Yuan, J. Li, L. Hou, X. Zhang, L. Shen, X.W. Lou, Adv. Funct. Mater. 22 (2012) 4592–4597.
- [44] B. Cui, H. Lin, Yz. Liu, Jb. Li, P. Sun, Xc. Zhao, Cj. Liu, J. Phys. Chem. C 113 (2009) 14083–14087.
- [45] M.C. Biesinger, B.P. Payne, A.P. Grosvenor, L.W.M. Lau, A.R. Gerson, R.S.C. Smart, Appl. Surf. Sci. 257 (2011) 2717–2730.
- [46] Z. Zhao, H. Wu, H. He, X. Xu, Y. Jin, Adv. Funct. Mater. 24 (2014) 4698–4705.
- [47] W. Setyawan, S. Curtarolo, Comput. Mater. Sci. 49 (2010) 299–312.
- [48] H. Yaghoubi, Z. Li, Y. Chen, H.T. Ngo, V.R. Bhethanabotla, B. Joseph, S. Ma, R. Schlaf, A. Takshi, ACS Catal. 5 (2015) 327–335.
- [49] J. Zhang, S. Liu, J. Yu, M. Jaroniec, J. Mater. Chem. 21 (2011) 14655–14662.
- [50] Y. Amit, Y. Li, A.I. Frenkel, U. Banin, ACS Nano 9 (2015) 10790–10800.
- [51] C. Xu, Y. Zhang, J. Chen, J. Lin, X. Zhang, Z. Wang, J. Zhou, Appl. Catal. B 204 (2017) 324–334.
- [52] K. Yang, W.Q. Huang, L. Xu, K.W. Luo, Y.C. Yang, G.F. Huang, Mater. Sci. Semicond. Process. 41 (2016) 200–208.
- [53] S. John, C. Soukoulis, M.H. Cohen, E.N. Economou, Phys. Rev. Lett. 57 (1986) 1777–1780.
- [54] R. Beranek, H. Kisch, Photochem. Photobiol. Sci. 7 (2008) 40–48.
- [55] A.G. Tamirat, W.-N. Su, A.A. Dubale, H.-M. Chen, B.-J. Hwang, J. Mater. Chem. A 3 (2015) 5949–5961.
- [56] J. Deng, X. Lv, J. Liu, H. Zhang, K. Nie, C. Hong, J. Wang, X. Sun, J. Zhong, S.-T. Lee, ACS Nano 9 (2015) 5348–5356.
- [57] X. Li, J. Yu, J. Low, Y. Fang, J. Xiao, X. Chen, J. Mater. Chem. A 3 (2015) 2485–2534.
- [58] L. Ge, C. Han, J. Liu, Appl. Catal. B 108–109 (2011) 100–107.
- [59] W. Zhen, X. Ning, B. Yang, Y. Wu, Z. Li, G. Lu, Appl. Catal. B 221 (2018) 243–257.
- [60] N. Seriani, C. Pinilla, Y. Crespo, J. Phys. Chem. C 119 (2015) 6696–6702.
- [61] G. Wang, B. Huang, Z. Li, Z. Lou, Z. Wang, Y. Dai, M.-H. Whangbo, Sci. Rep. 5 (2015) 8544.
- [62] Z. Zhang, J. Huang, M. Zhang, Q. Yuan, B. Dong, Appl. Catal. B 163 (2015) 298–305.
- [63] Y.C. Chen, T.C. Liu, Y.J. Hsu, ACS Appl. Mater. Interfaces 7 (2015) 1616–1623.
- [64] S. Chen, S. Shen, G. Liu, Y. Qi, F. Zhang, C. Li, Angew. Chemie Int. Ed. 127 (2015) 3090–3094.
- [65] A. Kudo, Y. Miseki, Chem. Soc. Rev. 38 (2009) 253–278.
- [66] S. Liu, J. Xia, J. Yu, ACS Appl. Mater. Interfaces 7 (2015) 8166–8175.
- [67] Y. Jiao, Y. Zheng, M. Jaroniec, S.Z. Qiao, Chem. Soc. Rev. 44 (2015) 2060–2086.
- [68] B. Hinemann, P.G. Moses, J. Bonde, K.P. Jorgensen, J.H. Nielsen, S. Hørch, I. Chorkendorff, J.K. Nørskov, J. Am. Chem. Soc. 127 (2005) 5308–5309.
- [69] J. Ran, G. Gao, F.T. Li, T.Y. Ma, A. Du, S.Z. Qiao, Nat. Commun. 8 (2017) 13907.